

**UCC Library and UCC researchers have made this item openly available.
Please [let us know](#) how this has helped you. Thanks!**

Title	Large block copolymer self-assembly for fabrication of subwavelength nanostructures for applications in optics
Author(s)	Mokarian-Tabari, Parvaneh; Senthamaraikannan, Ramsankar; Glynn, Colm; Collins, Timothy W.; Cummins, Cian; Nugent, David; O'Dwyer, Colm; Morris, Michael A.
Publication date	2017-04-05
Original citation	Mokarian-Tabari, P., Senthamaraikannan, R., Glynn, C., Collins, T. W., Cummins, C., Nugent, D., O'Dwyer, C. and Morris, M. A. (2017) 'Large Block Copolymer Self-Assembly for Fabrication of Subwavelength Nanostructures for Applications in Optics', Nano Letters, 17(5), pp. 2973-2978. doi: 10.1021/acs.nanolett.7b00226
Type of publication	Article (preprint)
Link to publisher's version	http://pubs.acs.org/doi/abs/10.1021/acs.nanolett.7b00226 http://dx.doi.org/10.1021/acs.nanolett.7b00226 Access to the full text of the published version may require a subscription.
Rights	© 2017 American Chemical Society. This document is the Accepted Manuscript version of a Published Work that appeared in final form in Nano Letters, copyright © American Chemical Society after peer review and technical editing by the publisher. To access the final edited and published work see https://pubs.acs.org/doi/pdf/10.1021/acs.nanolett.7b00226
Item downloaded from	http://hdl.handle.net/10468/6045

Downloaded on 2019-07-04T13:41:14Z

Large Block Copolymer Self-Assembly for Fabrication of Subwavelength Nanostructures for Applications in Optics

Parvaneh Mokarian-Tabari,^{†,‡,*} Ramsankar SenthamaraiKannan,^{†,‡} Colm Glynn,[‡] Timothy W. Collins,[‡] Cian Cummins,[†] David Nugent[†] Colm O'Dwyer,^{‡,§} and Michael A. Morris[†]

[†] Advanced Materials and BioEngineering Research Centre (AMBER) & CRANN, Trinity College Dublin, Ireland

[‡] Department of Chemistry, University College Cork, Cork, T12 YN60, Ireland

[§] Micro-Nano Systems Centre, Tyndall National Institute, Lee Maltings, Cork, T12 R5CP, Ireland

[†] Elucidare Limited, Unit 9 Caxton House, Great Cambourne, CB23 6JN, UK

Abstract

Nanostructured surfaces are common in nature and exhibit properties such as antireflectivity (moth eyes), self-cleaning (lotus leaf), iridescent colors (butterfly wings) and water harvesting (desert beetles). We now understand these properties and can mimic some of these natural structures in the laboratory. However, these synthetic structures are limited since they are not easily mass produced over large areas due to the limited scalability of current technologies such as UV-lithography, the high cost of infrastructure and the inability to pattern non-planar surfaces. Here, we report a solution process based on block copolymer (BCP) self-assembly to fabricate sub-wavelength structures on large areas of optical and curved surfaces with feature sizes and spacings designed to efficiently scatter visible light. Si nanopillars (SiNPs) with

diameters of $\sim 115 \pm 19$ nm, periodicity of 180 ± 18 nm and aspect ratio of 2-15 show a reduction in reflectivity by a factor of 100, $< 0.16\%$ between 400-900 nm at AOI 30° . Significantly, the reflectivity remains below 1.75% up to incident angles of 75° . Modelling the efficiency of a SiNP PV suggests a 24.6% increase in efficiency - representing a 3.52% (absolute) or 16.7% (relative) increase in electrical energy output from the PV system compared to the AR-coated device.

KEYWORDS: Subwavelength nanostructures, antireflective surfaces, reflectivity, omnidirectional, graded refractive index, block copolymers, optics.

Block copolymer (BCP) self-assembly is a potential solution based process that could offer an alternative route to produce highly ordered photonic crystal structures. However, BCP efforts have been limited to sub-100 nm spacing/feature sizes limiting their application in optics industry. BCPs generally form nanodomains of 5-100 nm due to microphase separation of incompatible constituent blocks. The size and structural arrangement of the domains can be customized by the molecular weight and volume fraction of the blocks. These BCP derived nanostructures have been employed for the fabrication of 1D photonic crystals^{1,2} based on lamellar systems, to 2D³ and 3D structures based on bicontinuous gyroid structures⁴, photonic gels^{5,6}, moth-eye structures⁷, higher luminescent LEDs⁸, antireflective coatings⁹ some with improved self-cleaning properties¹⁰ and metamaterials^{11,12}. However, advancing the technology beyond 1D and 2D photonic crystals for manipulation of visible light has been challenging¹³. In order to modulate photons in the visible and near-infrared light range (400-1500 nm), lateral pattern feature/domain sizes must ensure a periodicity, graded index and aspect ratio that minimizes broadband reflectivity, and ideally maintain reflectivity suppression so the effect is omnidirectional. The diameter of the features being subwavelength strongly affect reflectivity (close to quarter wavelength, but not prescriptively so). The smaller features do not suppress the reflectivity as much as the larger features do. See Figure S1. There is thought

to be an ‘inherent size limitation’ in BCP self-assembly due to significant kinetic penalties that arise from higher molecular entanglement in ultra-high molecular weight polymers (>500 kg/mol), requiring a very long annealing time^{14,15}. Furthermore, synthesising ultra-high molecular weight BCPs above 500,000 kg/mol of the required monodispersity remains very challenging^{15,16}. Alternative strategies to increase domain dimensions such as adding homopolymers¹⁷ and swelling the domains with ionic liquid¹⁸ have been explored, but they introduce defects, segregation or simply do not go beyond 100 nm limit. This paper addresses the critical element of the work extending the size limitations of BCPs from the sub-20 nm range (as developed for semiconductor fabrication) to 100 nm¹⁶ and toward dimension ranges expected for techniques applicable to the optics industry. Here, we exploit commercially available block copolymers to generate periodic hexagonal domain structures with average cylinder diameter of 115 nm and the inter cylinder spacing (L_0) of greater than 160 nm, and use these masks to make nanopillars of high aspect ratio for fabrication of omnidirectional broadband antireflective surfaces. We show our 870 nm tall SiNPs with a tapered structure and height: width aspect ratio >10, suppress reflectivity more than 2 orders of magnitude, and from 34% to 0.16% in the range of visible light. To date, we believe this is the minimum reflectance of nanotextured Si made by BCPs^{19,20} and comparable with other methods rivaling black silicon.²¹ Also as we show here, this method has the potential to be used for patterning curved surfaces.

Nanopattern formation and BCP characterization. A highly periodic BCP pattern was made using commercially available poly(styrene-*b*-2-vinylpyridine) (PS-*b*-P2VP) with molecular weight of about 800 kg/mol, phase separating into cylinders with diameter of 115±19 nm, and periodicity of 180±18 nm on Si, GaN and glass (Figure 1(a-c)). Figures 1(d-f) show the top-down SEM images of various nanopillars with an excellent coverage over large substrate areas after pattern transfer. The expected very slow kinetics for ordered microphase separation of

high molecular weight BCPs were not observed, and solvent annealing for an hour (THF/CHCl₃ at room temperature) led to the formation of highly ordered hexagonally packed domain patterns of feature size > 100 nm (for more details see Methods, Supporting Information). Due to slow reptation of the ultra-high molecular BCP chain ($M_w > 500$ kg/mol), this is a highly unexpected observation. To the best of our knowledge, to achieve a highly ordered pattern in the range of molecular weight presented in this article (*i.e.* 800 kg/mol) either requires hours^{14,15} and weeks^{1,13} of annealing at higher temperatures or involves special polymerization methods.²² Most probably, the system seems likely to have been trapped in a kinetically metastable phase within the thin film. We suggest that a meta-stable hexagonally perforated lamellar (HPL) phase is formed in these thin films due to a confinement effect seen in other systems²³. Longer annealing durations (2-24 hours) does result in either a reduction or complete loss of order in the pattern (see Figure S2), while the film remains intact on the substrate (*i.e.* no dewetting is observed). This suggests the original phase separated pattern was possibly a non-equilibrium phase rather than an equilibrium state. However, this might be an overly simplistic view as recent papers have shown that solvent annealing is a complex process with kinetic and thermodynamic limitations that might enable more rapid ordered microphase separation than expected²⁴⁻²⁶.

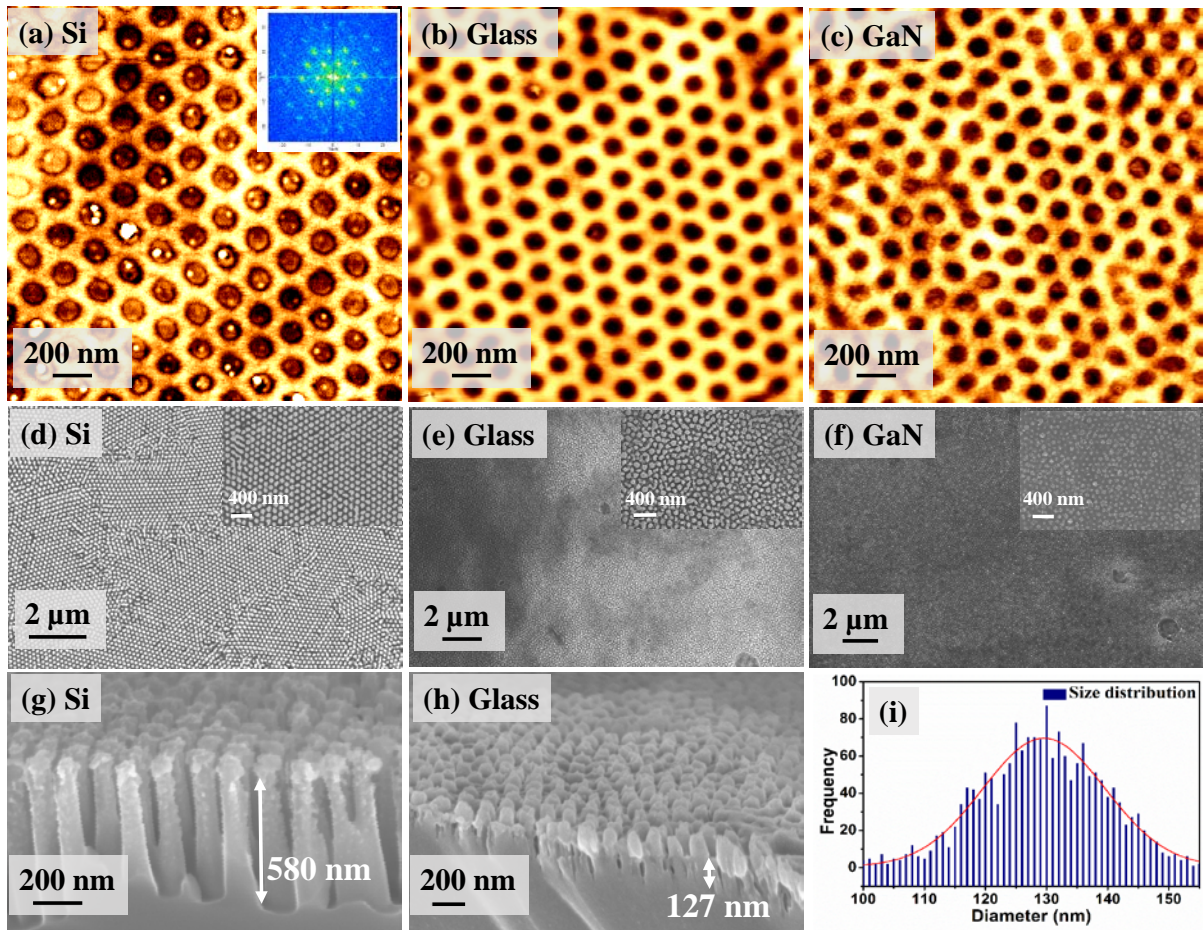


Figure 1. Large domain (diameter > 100 nm) of (PS-*b*-P2VP) on optical surfaces. AFM topography of the phase separated polymer film on (a) Si with the FFT profile on inset, (b) BK7 glass, and (c) GaN. SEM top-down images of (d) Si nanopillars (e) glass and (f) GaN nanopillars after etch and pattern transfer. Cross section SEM image of (g) Si, and (h) glass nanopillars. (i) Size distribution of the domains (diameter of the cylinders) of the polymer pattern on Si.

To obtain more insight about the internal structure of the film, FIB-lamella cross section TEM and STEM was performed on the polymer film after solvent annealing. Substrates were stained with RuO₄ for PS (Figure 2b), and iodine (Figure 2c) for P2VP to enhance the contrast between PS and P2VP domains for imaging. Figure 2a shows a STEM-EDX elemental map of the features in the iodine stained film. Figure 2c shows a perforated structure suggests the

formation of a HPL phase with stacking layers of the ABC type (since the centre of the cylinders in the first layer is offset against the lower layer (Figure 2d)). A 3D modelling of the structure for visualisation is presented in (Figure 2e). A video of the modelled structure is provided in Supporting Information (Figure S3). We have studied a wide range of film thickness from 25 to 500 nm with solvent annealing time of 1-24 h (see Figure S2). The best result is mostly achieved at a narrow window of thickness close to the pitch of 165 nm and within an hour of exposure to THF and CHCl_3 with ratio of (2:1).

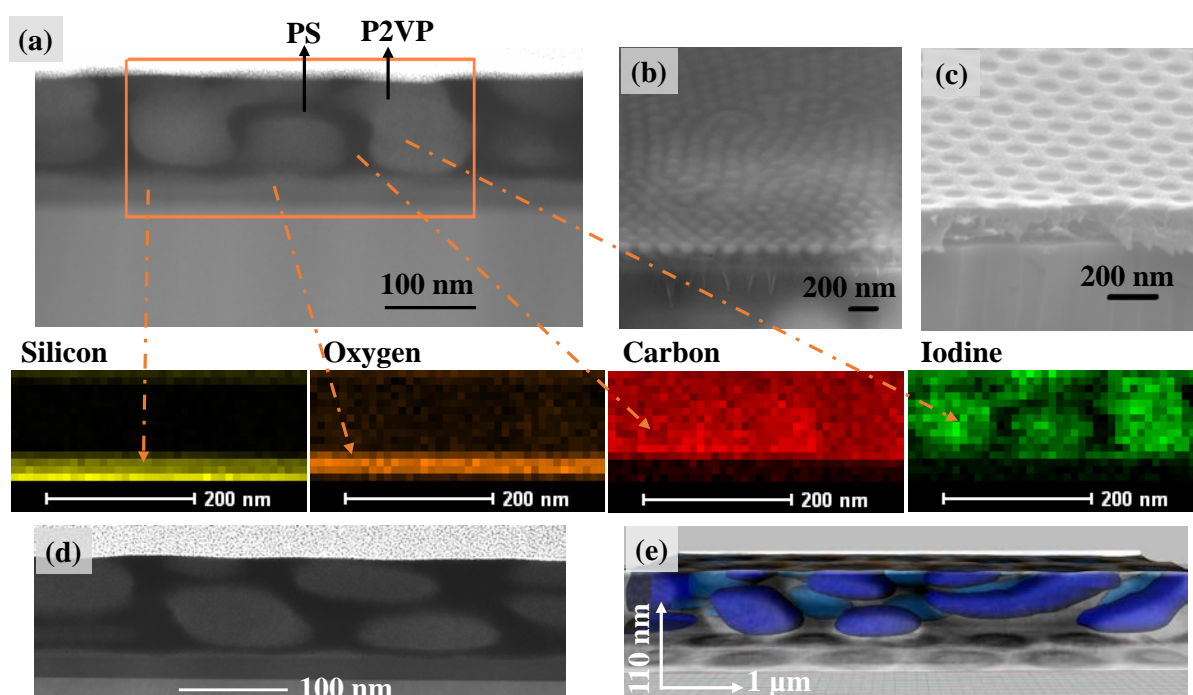


Figure 2. Internal structure of the perforated lamellae in 800k g/mol PS-*b*-P2VP. (a) FIB-lamella STEM cross section of the film after annealing and staining with iodine, and the relevant EDX map, (b) after staining the film with iodine, and (c) after staining with RuO_4 . (d) FIB-STEM image of polymer film after annealing and staining with iodine showing the perforated lamellar and ABC stacking order, (e) visualization of the 3D reconstructed structure based on STEM-LAM cross section and AFM images. For clarity P2VP domains are colored in purple in the front plane and blue at the back plane, while PS domains are transparent.

Optical characterization. The BCP template in (Figure 1a) was used as a mask to make SiNPs with aspect ratio of 2-15 and with heights up to 1150 nm. As a proof of concept a BK7 convex lens with diameter of 3.2 cm was also patterned by BCPs (Figure S4). The subwavelength patterns made by BCP self-assembly were transferred to a number of electronic, industrial and optoelectronic substrates such as Si, glass and GaN after metal oxide inclusion²⁷ and by plasma etch. Figure 3 shows the average reflectivity of our “super tall” SiNPs with apex and base diameter of 70 and 130 nm respectively and height of 870 nm within the angle of incidence range of 30-75°. The significance of the result shown in (Figure 3) is the reduction in reflectivity by a factor of >100 achieved by overcoming the 100 nm size limit in block copolymers. To date, the state-of-the-art (SOA) antireflective properties of sub-wavelength structures derived from BCPs has an average reflectivity of about 1% at best¹⁹ and often above 1%. In comparison, we achieved a broadband antireflection less than 0.16%, over the entire spectrum of 400-900 nm at angle of incidence (AOI) of 30° with our 870 nm high SiNPs (Figure 3a). The advance in the SOA can be shown by reference to recent work by Rahman *et al*¹⁹, for smaller domain size (sub 50 nm) and shorter nanopillars (made by BCPs), the average value of reflectivity is 20% at higher AOIs¹⁹, while for our samples the average reflectivity remains as low as 1.74% at AOI as high as 75°, across the Vis-NIR (visible- near infrared) range (Figure 3). The marked reduction in visible light reflectivity from the BCP periodically patterned textured Si surface results from scattering in the Vis-NIR range, as Fresnel reflection and reflectivity from step-changes in refractive index are significantly reduced. It should be mentioned although the formation of giant lamella pattern with $L_0 \sim 200$ nm has been demonstrated¹⁴, they do not provide the graded refractive index and index matching with the ambient air (cause by SiNP tapering) to provide an effective medium, needed for enhanced suppression of light reflectivity.

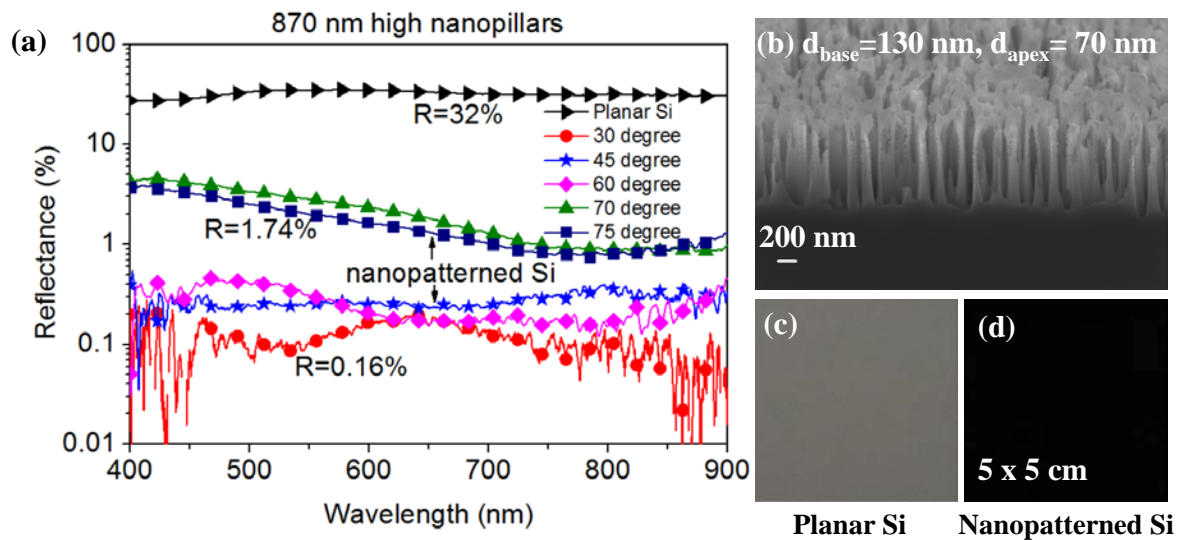


Figure 3. Broadband antireflection properties of silicon nanopillars by block copolymer self-assembly 30-75°. (a) reflectivity of planar Si (black triangles) and 870 nm SiNPs for different values of AOI: 30° (red circle), 45° (blue star), 60° (pink diamond), 70° (green triangle), 75° (navy square), (b) the SEM cross section image of SiNPs with a height of 870 nm, base diameter of 130 nm and apex diameter of 70 nm. (c) Highly reflective planar Si and (d) photographs of nanopatterned Si that appears uniformly black by elimination of visible light reflection compared to Si (100) substrate.

Omnidirectional broadband antireflective SiNPs. The height and angle dependent optical reflectance of the Si nanopillars was probed in the 400 – 900 nm wavelength for AOIs from near-normal incidence to 75°. Geometric features of the Si nanopillars are characterised and shown in (Figure 4a-f). While the periodicity of the nanopatterns remains the same for all samples, the height of the pillars is varied by BCP processing and etching from 180 to 1150 nm. Tuning the height with high fidelity through our metal oxide inclusion²⁷ is not achievable through the wet etch process or polymer masks only. The nanopillars sidewall are consistently in the range 12-15° for the period array. The general trend in reflectivity is maintained for all AOIs (Figure 4g-4j), and by tuning the height of the nanopillars from 180 to 870 nm, we can

suppresses the reflectivity more efficiently, as expected due to graded refractive index effect in tall nanopillars with a reducing volume fraction further from the substrate. Increasing the aspect ratio of the SiNPs increase the optical length of the incident light which can lead to multiple reflection and scattering which subsequently can leads to more absorption. However, there appears to be a threshold height (~870 nm) above which there is no significant change in reflectivity (compare data for 870 nm nanopillars and 1150 nm nanopillars in Figure 4; see also Figure 3a). A similar effect has been reported²⁸, in which increasing the height of the pillars leads to an increase in reflectivity while the opposite effect is expected. Due to their large surface area, the nanopillars are susceptible to deformation due to surface forces, such as adhesive and capillary force. During the dry etch process, greater capillary force for the high aspect ratio nanopillars, overcomes the supportive force²⁸, leading SiNPs to bend and aggregate at the top which acts as a reflective surface. The SEM image (Figure 4f) confirms the aggregation of SiNPs on top for the tallest SiNP (1150 nm), explaining the reason for lower reflectivity in comparison to 870 nm SiNPs, which exhibits the strongest reduction in reflectivity (0.16-1.74%) at all angles of incidences (Figure 4). The minimum angular dependency demonstrated here could have a significant impact on photovoltaics efficiency as it would reduce the need for an integrated mechanised tracking system that keeps the solar cells aligned to the sun throughout the day.

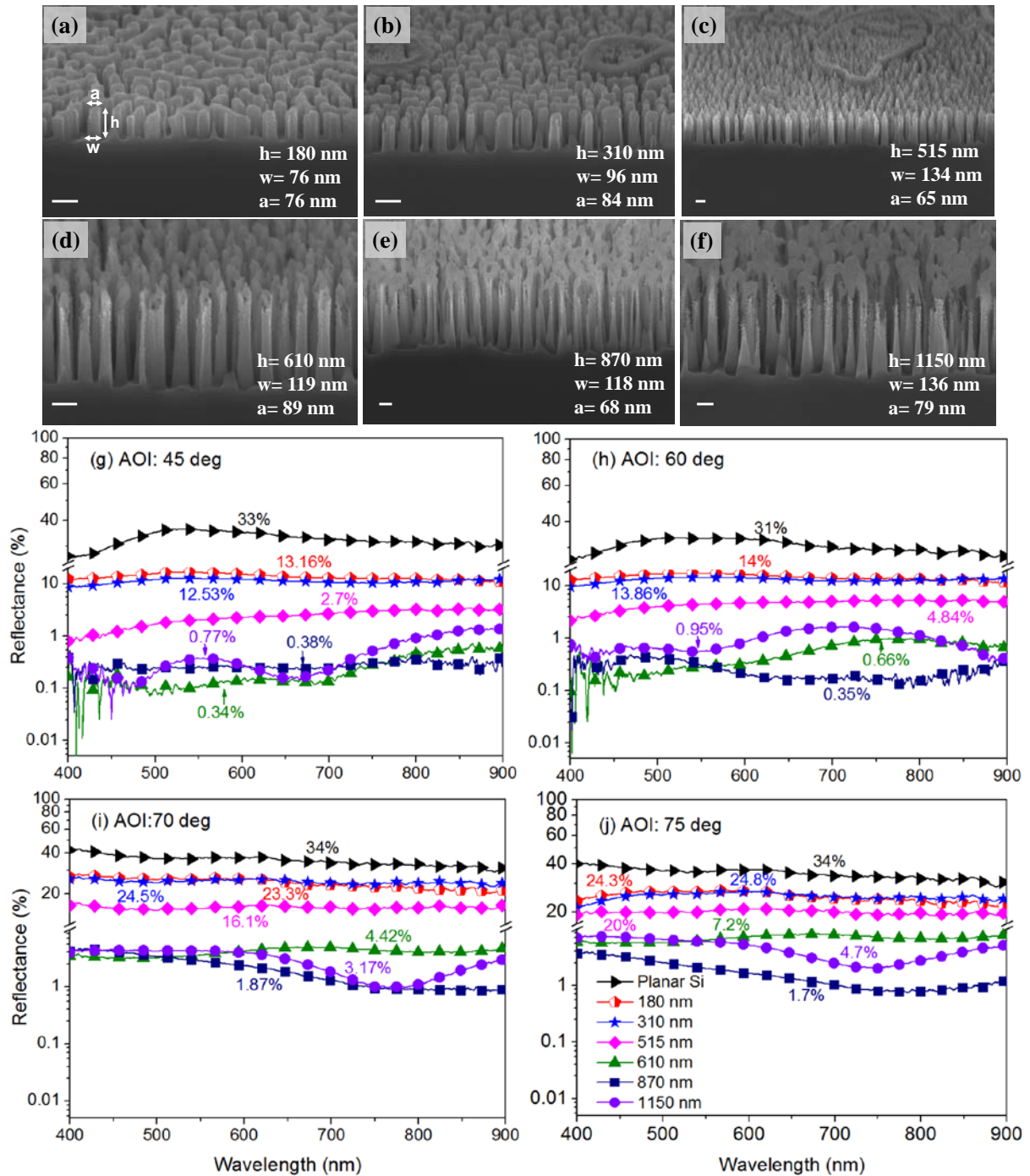


Figure 4. Omnidirectional broadband antireflective SiNPs with aspect ratio of 2-15. Geometry configuration of highly tuneable SiNPs made by large BCPs with relevant heights at (a) 180 nm, (b) 310 nm, (c) 515 nm, (d) 610 nm, (e) 870 nm and (f) 1150 nm. The scale bars are 200 nm. Angular dependence of SiNPs with various height at different angle of incidence: (g) 45°, (h) 60°, (i) 70° and (j) 75°. Note that the y-axis is logarithmic scale for the nanopatterned Si

data (up to the break point) and linear scale for planar Si. The legend in (g-j) demonstrate average SiNP's height.

Angle-resolved reflectance data in (Figure 5) demonstrate that BCP-nanopatterned silicon surfaces are very effective in reducing silicon transparency at IR wavelengths, in particular for common data transmission wavelengths of 1310 and 1550 nm (Figure 5a and 5b) from Si/SiGe-based MQW LEDs²⁹ or InGaAs/GaAs lasers³⁰. The patterned tapered SiNP structures with a periodicity of ~ 180 nm ($\sim \lambda/2n$), comprising a graded index effective medium with a height $h \sim \lambda/2$ (i.e. 610 nm pillars at $\lambda = 1310$ nm), reduces NIR reflectivity down to 7.5-15% from 44% in non-patterned Si within the AOI range of 30-75° (Figure 5a) consistent with a very effective subwavelength broadband omnidirectional antireflection coating. In the visible range, at the He-Ne emission energy at $\lambda = 632.8$ nm (Figure 5d), resonant scattering is considerably enhanced for 610 nm, with maximum antireflection (down to a value as low as 0.15 - 8%) up to 75° away from normal incidence. In the visible range (at 514.5 nm and 632.8 nm) NP with heights from 870 - 1150 nm high NPs exhibit the best broadband omnidirectional antireflection properties, and both cases exhibit aspect ratios from 10-15. The minimum reflectivity of 0.16-1.74% at $\lambda = 632.8$ nm is achieved for 870 nm high SiNPs (aspect ratio > 10). SiNPs antireflection characteristics broadband frequencies within visible range at high aspect ratios for deeply subwavelength diameter and periodicity. In the NIR range, shorter NPs (lower aspect ratio for similar periodicity and diameters, are effect antireflection coatings when $h \sim \lambda/2$.

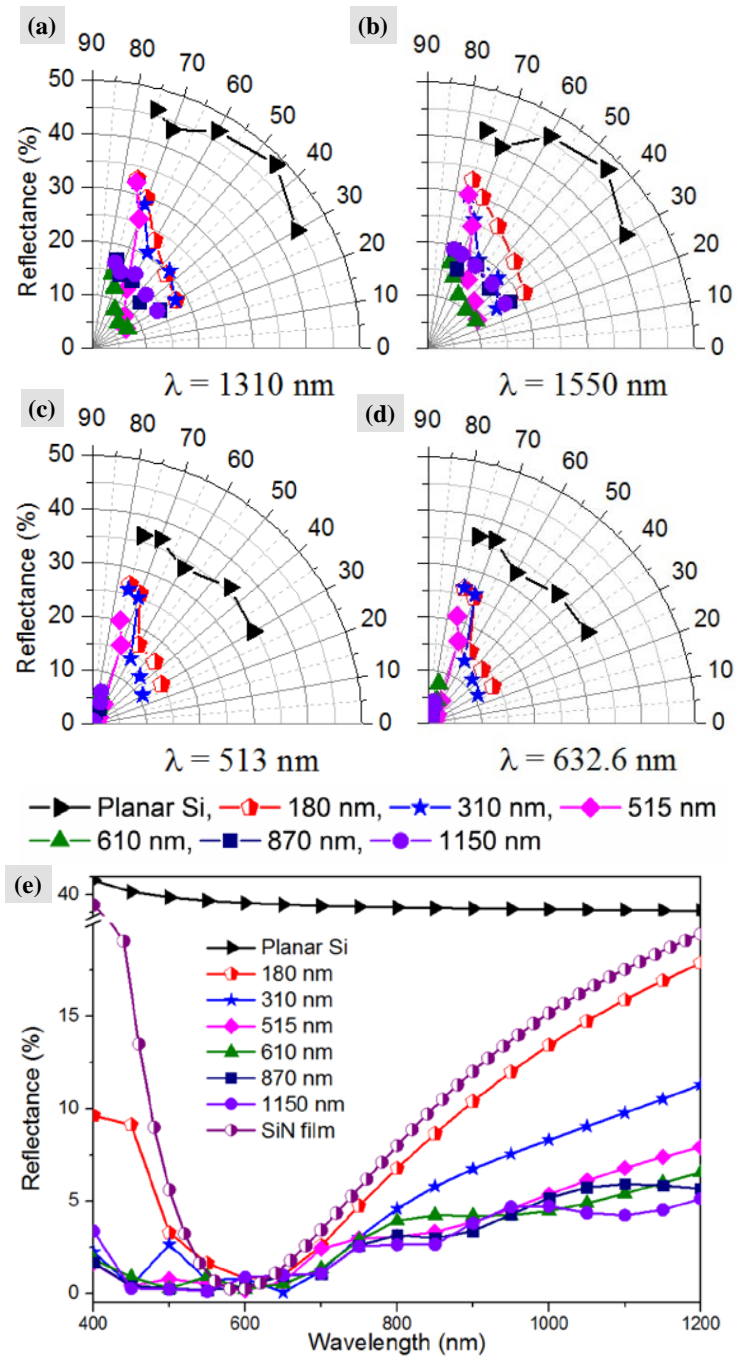


Figure 5. Angular reflectivity plot (0-90°) of SiNPs with different heights. At (a) $\lambda = 1310$ nm, (b) $\lambda = 1550$, (c) $\lambda = 513$ nm and (d) $\lambda = 632.6$ nm. The legends and colors demonstrate SiNP's height. (e) Simulated reflectance spectra of unpolarised light from nanopillars with different pillar heights compared to planar Si and SiN coated (75-nm layer) silicon.

Simulation. We have simulated the normal reflectance of unpolarised light from the SiNP layers across the solar emission spectrum (400 to 1200 nm) using GD-Calc, which computes diffraction efficiencies of optical grating structures, including bi-periodic gratings. For more information see the SI document and (Figure S7). These results are compared with the Fresnel reflectance from uncoated silicon and SiN-coated silicon in Figure 5e. Applying simulated reflectance results to the AM1 (overhead midday) solar spectrum and standard model for photon absorption in monocrystalline silicon (fill factor = 0.55), the predicted conversion efficiency of a PV panel would increase from 17.33% for untreated silicon, to 22.09% for 870 nm SiNPs. Reflectance values for an AR coating (75 nm SiN film) are also calculated and imply an efficiency of 21.08%. Hence, the SiNPs presented in this paper would improve the electrical output of a silicon PV system by 1.01% (absolute) or 4.79% (relative) compared to an AR-coated device. As noted previously, however, measured reflectance values are considerably lower than simulated results. The most likely cause of this anomaly is the presence of a thin silicon oxide layer coating over the silicon nanopillars. Formed during the plasma etch process, this layer reduces reflections at the high-RI silicon interface. Assuming a uniform thickness along the length of the nanopillar, the SiO₂ layer will have a greater influence on the localised refractive index at the top of the pillar than at the bottom. The net effect is an additional gradation in the refractive index experienced by light diffracting through the structure and thereby a reduced reflectivity. Applying measured reflectance values to the PV model suggests a PV efficiency of 24.6% - representing a 3.52% (absolute) or 16.7% (relative) increase in electrical energy compared to the AR-coated device.

In conclusion, the BCP patterning capabilities described here make exceptional coatings for improved transparency, light focusing, antireflection and for tuning photon absorption for a variety of applications on a wide range of surfaces, materials and non-planar substrates. BCP patterning that avoid previous ‘inherent’ size limitations, that facilitate a high

density ordered array of nanopillars with tunable height, are easily scalable and can be formed at low temperature. Compared to nanocones and other 'black' silicon layers, broadband antireflection coatings may now be possible for flexible PVs, solar cell technologies, and for broadband elimination of reflection of high quality glass optics.

ASSOCIATED CONTENT

Supporting Information

A video link for the visualization of the 3 model, additional figures, methods including film preparation, pattern transfer, optical analysis, dimensional analysis and microscopy are available free of charge via the Internet at <http://pubs.acs.org>.

AUTHOR INFORMATION

Corresponding Author

*E-mail: mokariap@tcd.ie, Tel: +353 1 896 3087.

Present Address

*Advanced Materials and BioEngineering Research (AMBER) Centre & CRANN, Trinity College Dublin, Ireland

Author contributions

PM coordinated the research project. RS performed the block copolymer experiments and AFM, SEM, STEM and EDAX. CG and COD performed the optical characterizations, Vis-IR and angle dependant experiments. TWC worked on 3D modelling, and developed a software for calculating the size distribution in the pattern. CC has performed the FIB-TEM work. PM, COD, DN and MAM discussed and interpreted the data and the results. PM, COD and MAM co- wrote the paper.

Notes

The authors declare no competing financial interest.

ACKNOWLEDGEMENTS

We acknowledge the financial support from Enterprise Ireland (Commercialisation Fund-CF/2014/ /4055) and Science Foundation Ireland (SFI AMBER 12/RC/2278). We would like to thanks Mr Alan Hyde from Tyndall National Institute for providing etch expertise. The authors would like to thank Dr. Eoin McCarthy in Advanced Microscopy Laboratory (AML), in CRANN Institute for assistance in STEM-EDAX mapping and imaging. We would like to

thanks Dr. Colm Coughlan (currently in Dublin Institute for Advanced Studies) for his assistance in software development.

REFERENCES:

1. Urbas, A. M.; Maldovan, M.; DeRege, P.; Thomas, E. L. *Adv. Mater.* **2002**, *14*, 1850-1853.
2. Sveinbjornsson, B. R.; Weitekamp, R. A.; Miyake, G. M.; Xia, Y.; Atwater, H. A.; Grubbs, R. H. *Proc. Natl. Acad. Sci. U. S. A.* **2012**, *109*, 14332-14336.
3. Deng, T.; Chen, C. T.; Honeker, C.; Thomas, E. L. *Polymer* **2003**, *44*, 6549-6553.
4. Hajduk, D. A.; Harper, P. E.; Gruner, S. M.; Honeker, C. C.; Kim, G.; Thomas, E. L.; Fetters, L. J. *Macromolecules* **1994**, *27*, 4063-4075.
5. Valkama, S.; Kosonen, H.; Ruokolainen, J.; Haatainen, T.; Torkkeli, M.; Serimaa, R.; Ten Brinke, G.; Ikkala, O. *Nature Materials* **2004**, *3*, 872-876.
6. Chiang, Y. W.; Chou, C. Y.; Wu, C. S.; Lin, E. L.; Yoon, J.; Thomas, E. L. *Macromolecules* **2015**, *48*, 4004-4011.
7. Lohmuller, T.; Helgert, M.; Sundermann, M.; Brunner, R.; Spatz, J. P. *Nano Letters* **2008**, *8*, 1429-1433.
8. Fujimoto, A.; Asakawa, K. *J. Photopolym Sci. Technol.* **2007**, *20*, 499-503.
9. Zhang, X.; Sushkov, A. B.; Metting, C. J.; Fackler, S.; Drew, H. D.; Briber, R. M. *Plasma Process. Polym.* **2012**, *9*, 968-974.
10. Guldin, S.; Kohn, P.; Stefik, M.; Song, J.; Divitini, G.; Ecarla, F.; Ducati, C.; Wiesner, U.; Steiner, U. *Nano Letters* **2013**, *13*, 5329-5335.
11. Hur, K.; Francescato, Y.; Giannini, V.; Maier, S. A.; Hennig, R. G.; Wiesner, U. *Angew. Chem.-Int. Edit.* **2011**, *50*, 11985-11989.
12. Vignolini, S.; Yufa, N. A.; Cunha, P. S.; Guldin, S.; Rushkin, I.; Stefik, M.; Hur, K.; Wiesner, U.; Baumberg, J. J.; Steiner, U. *Adv. Mater.* **2012**, *24*, OP23-OP27.
13. Stefik, M.; Guldin, S.; Vignolini, S.; Wiesner, U.; Steiner, U. *Chem. Soc. Rev.* **2015**, *44*, 5076-5091.
14. Kim, E.; Ahn, H.; Park, S.; Lee, H.; Lee, M.; Lee, S.; Kim, T.; Kwak, E. A.; Lee, J. H.; Lei, X.; Huh, J.; Bang, J.; Lee, B.; Ryu, D. Y. *Acs Nano* **2013**, *7*, 1952-1960.
15. Mapas, J. K. D.; Thomay, T.; Cartwright, A. N.; Ilavsky, J.; Rzaev, J. *Macromolecules* **2016**, *49*, 3733-3738.
16. Runge, M. B.; Bowden, N. B. *Journal of the American Chemical Society* **2007**, *129*, 10551-10560.
17. Urbas, A.; Sharp, R.; Fink, Y.; Thomas, E. L.; Xenidou, M.; Fetters, L. J. *Adv. Mater.* **2000**, *12*, 812-814.
18. Noro, A.; Tomita, Y.; Shinohara, Y.; Sageshima, Y.; Walish, J. J.; Matsushita, Y.; Thomas, E. L. *Macromolecules* **2014**, *47*, 4103-4109.
19. Rahman, A.; Ashraf, A.; Xin, H. L.; Tong, X.; Sutter, P.; Eisaman, M. D.; Black, C. T. *Nat. Commun.* **2015**, *6*, 6.
20. Paivanranta, B.; Sahoo, P. K.; Tocce, E.; Auzelyte, V.; Ekinci, Y.; Solak, H. H.; Liu, C. C.; Stuenkel, K. O.; Nealey, P. F.; David, C. *Acs Nano* **2011**, *5*, 1860-1864.
21. Raut, H. K.; Ganesh, V. A.; Nair, A. S.; Ramakrishna, S. *Energy Environ. Sci.* **2011**, *4*, 3779-3804.
22. Yoon, J.; Mathers, R. T.; Coates, G. W.; Thomas, E. L. *Macromolecules* **2006**, *39*, 1913-1919.
23. Pester, C. W.; Schmidt, K.; Ruppel, M.; Schoberth, H. G.; Boker, A. *Macromolecules* **2015**, *48*, 6206-6213.
24. Mokarian-Tabari, P.; Cummins, C.; Rasappa, S.; Simao, C.; Sotomayor Torres, C. M.; Holmes, J. D.; Morris, M. A. *Langmuir : the ACS journal of surfaces and colloids* **2014**, *30*, 10728-39.
25. Baruth, A.; Seo, M.; Lin, C. H.; Walster, K.; Shankar, A.; Hillmyer, M. A.; Leighton, C. *ACS Appl. Mater. Interfaces* **2014**, *6*, 13770-13781.
26. Lundy, R.; Flynn, S. P.; Cummins, C.; Kelleher, S. M.; Collins, M. N.; Dalton, E.; Daniels, S.; Morris, M. A.; Enright, R. *Physical Chemistry Chemical Physics* **2017**, *19*, 2805-2815.
27. Ghoshal, T.; Maity, T.; Godsell, J. F.; Roy, S.; Morris, M. A. *Adv. Mater.* **2012**, *24*, 2390-2397.

28. Teng, F.; Li, N.; Liu, L. X.; Xu, D. R.; Xiao, D. Y.; Lu, N. *Rsc Advances* **2016**, *6*, 15803-15807.
29. O'Dwyer, C.; Szachowicz, M.; Visimberga, G.; Lavayen, V.; Newcomb, S. B.; Torres, C. M. S. *Nature Nanotechnology* **2009**, *4*, 239-244.
30. Bimberg, D.; Kirstaedter, N.; Ledentsov, N. N.; Alferov, Z. I.; Kopev, P. S.; Ustinov, V. M. *Ieee Journal of Selected Topics in Quantum Electronics* **1997**, *3*, 196-205.

Supporting Information

Large Block Copolymer Self-Assembly for Fabrication of Subwavelength Nanostructures for Applications in Optics

Parvaneh Mokarian-Tabari,^{†,‡,*} Ramsankar Senthamaraikannan,^{†,‡} Colm Glynn,[‡] Timothy W. Collins,[‡] Cian Cummins,[†] David Nugent,[†] Colm O'Dwyer,^{‡,§} and Michael A. Morris[†]

[†] Advanced Materials and BioEngineering Research Centre (AMBER) & CRANN, Trinity College Dublin, The University of Dublin, Ireland

[‡] Department of Chemistry, University College Cork, Cork, T12 YN60, Ireland

[†] Elucidare Limited, Unit 9 Caxton House, Great Cambourne, CB23 6JN, UK

[§] Micro-Nano Systems Centre, Tyndall National Institute, Lee Maltings, Cork, T12 R5CP, Ireland

*E-mail: mokariap@tcd.ie

The diameter of the features being subwavelength strongly affect reflectivity (close to quarter wavelength, but not prescriptively so). The smaller features do not suppress the reflectivity as much as the larger features do. See Figure S1.

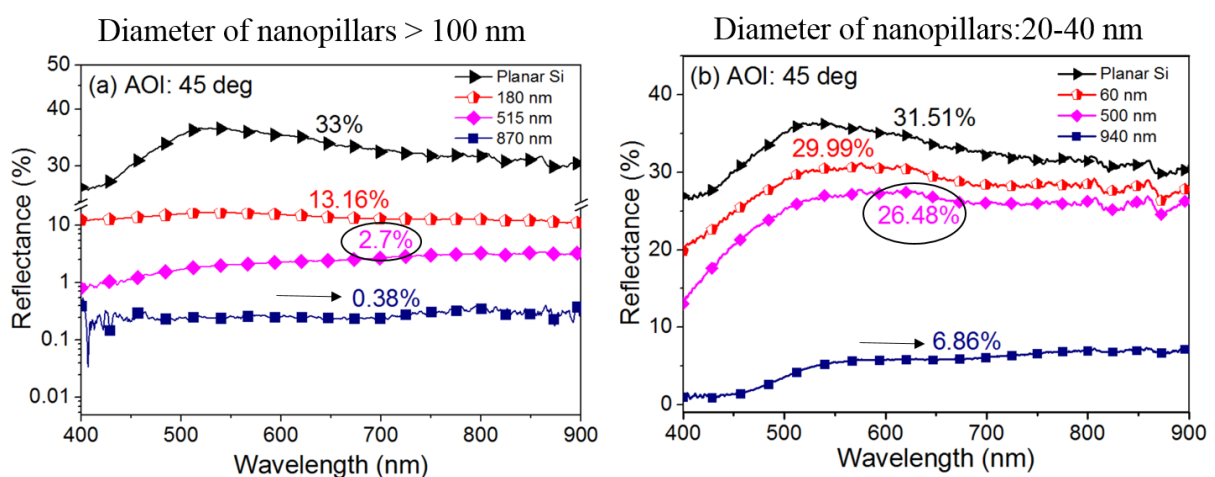


Figure S1. Comparing the reflectivity of (a) small nanopillars (diameter of 20-40 nm) with (b) large nanopillars (d>100 nm). Colors are indicative of nanopillars height. The large

dimensions nanopillars clearly suppress light reflection much more effectively. The colors are indicative of nanopillars height.

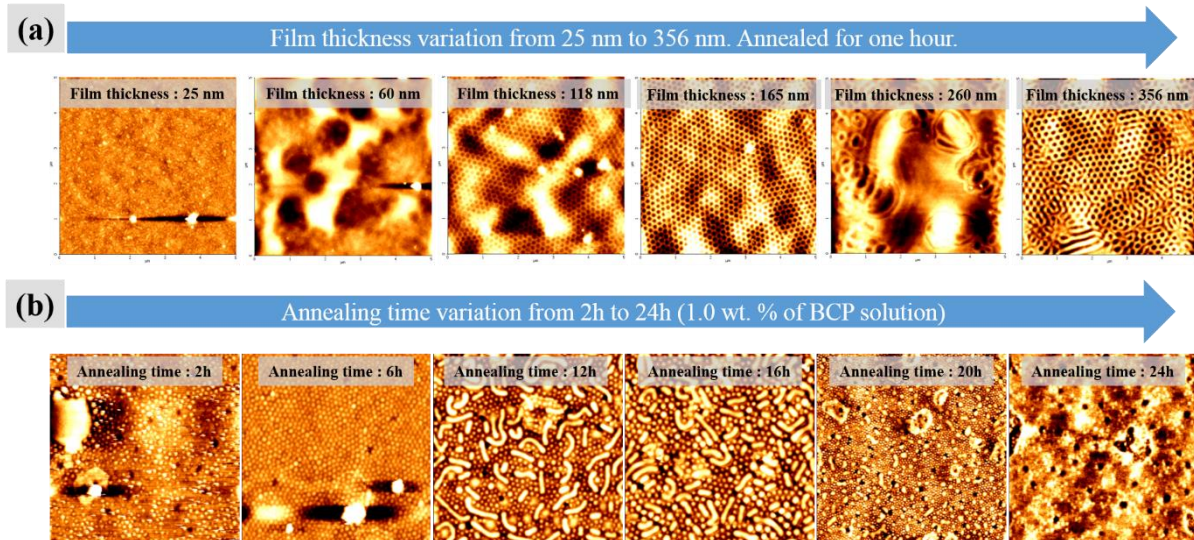


Figure S2. Film thickness and solvent annealing time variation. AFM topographic images of BCP films after solvent annealing. (a) Phase separation after an hour solvent annealing of films with a different thicknesses (b) annealing time from 2h to 24h for 1 wt. % BCP solution.

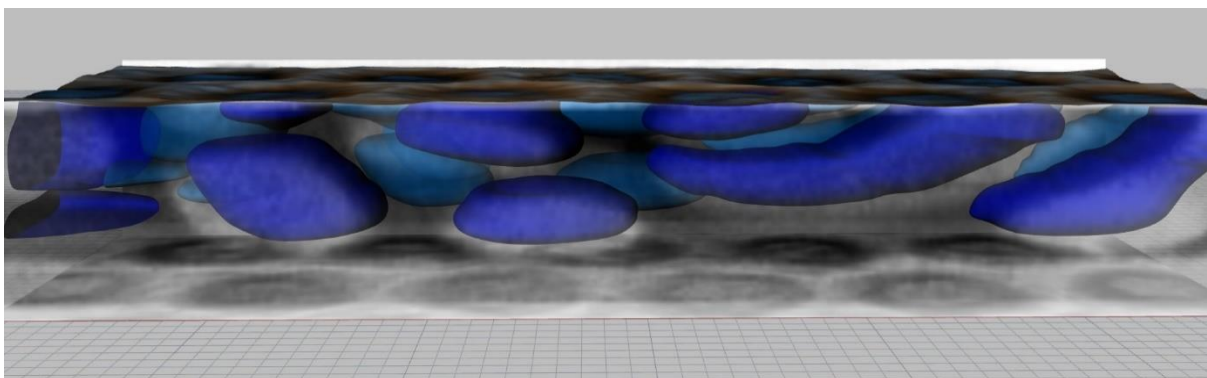


Figure S3. Visualization of the 3D modelled structure based on STEM-LAM cross section and AFM images. 3D modelled structure is constructed using the profile from STEM images and AFM images. The domains are colorised to show the layers of material. Link for the 3D video of the modelled structure: [Click here](#)

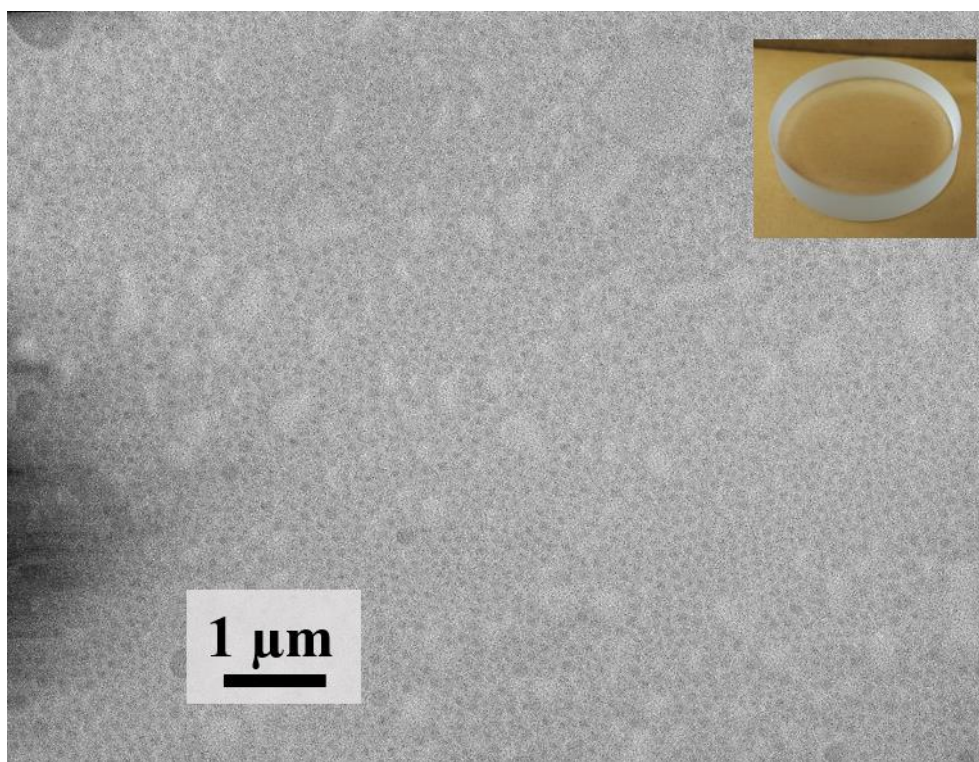


Figure S4. Patterned BK7 convex lens. SEM image of PS-*b*-P2VP after phase separation on BK7 convex lens. 2.0 wt. % of PS-*b*-P2VP polymer solution was spin coated on convex lens and exposed to mixed solvent of THF:CHCl₃ with volume ratio of 2:1, for an hour at room temperature. Phase separated BCP thin film were stained in iodine for 6 hours to enhance the contrast difference between PS and P2VP block and image them in SEM. The inset is the optical micrograph of the lens.

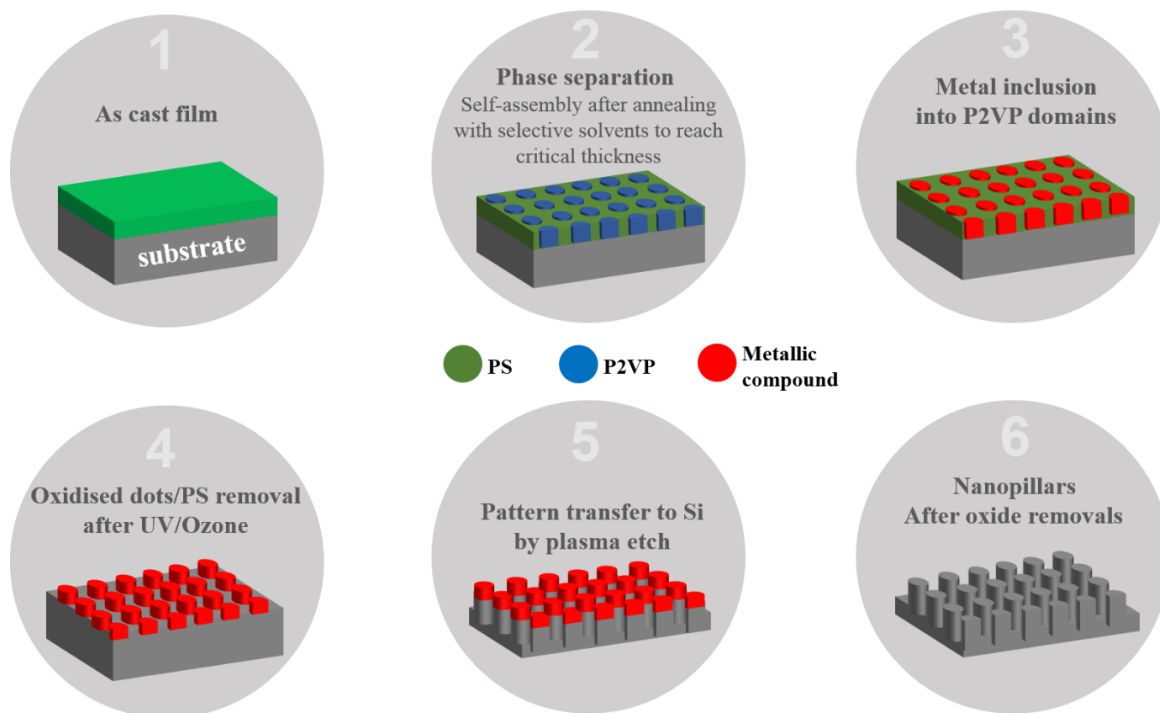


Figure S5. Schematic representation of fabrication of nanopatterned Si.

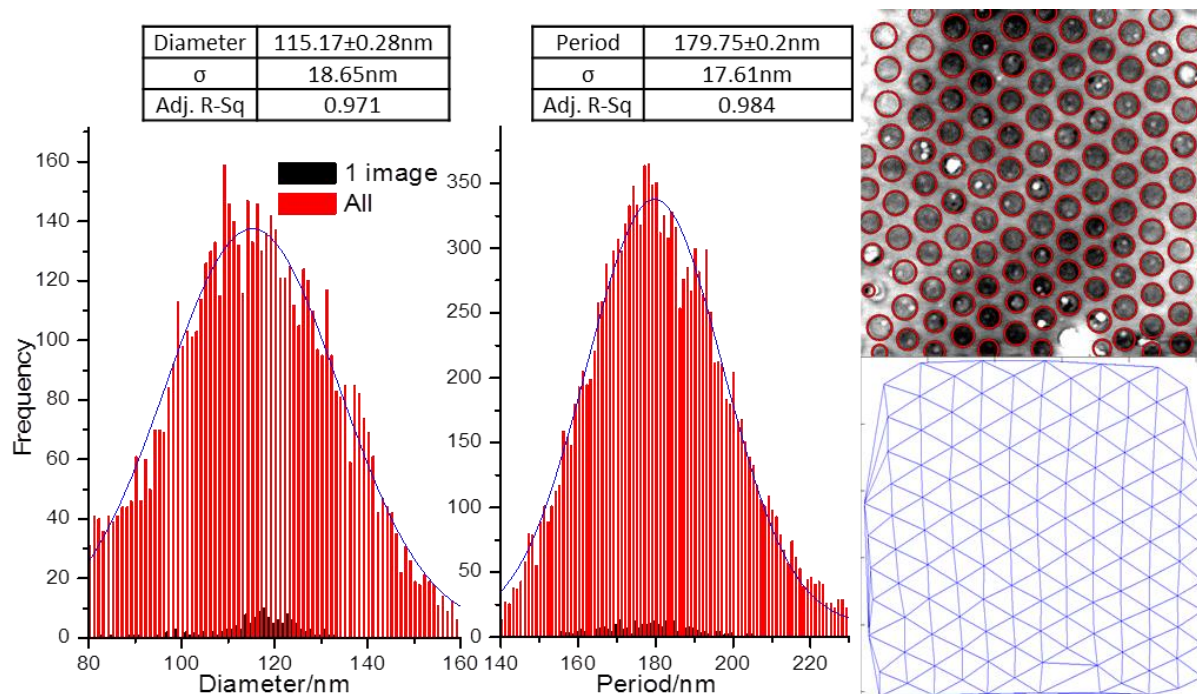


Figure S6. Size distribution for cylinder diameter (CD) (left) and period (L_0) (right) of the BCP films made on Si. Data was collected from 17 images of 10 individual samples. An example of the output detected features and Delaunay triangulation are also shown.

Methods

Film preparation. PS-*b*-P2VP ($M_n = 440.0$ - b - 353.0 kg/mol, PDI: 1.19) was purchased from Polymer Source. The polymer was dissolved in a toluene:tetrahydrofuran (THF) (80:20) mixture to yield 0.5 - 3.0 wt% solutions, and left stirring for 2 h to ensure complete dissolution. BCP films were prepared by spin coating the polymer solution onto the substrates at 4500 rpm for 30 s. Following deposition, the PS-*b*-P2VP films were exposed to mixed solvents of THF:CHCl₃ with volume ratio of 2:1, for an hour at room temperature. Solvent annealing was carried out in the conventional manner with two small vials containing 2 ml THF and 1 ml CHCl₃ placed inside a glass jar with volume of approximately 150 ml, along with the BCP sample. Phase separated BCP thin film were reconstructed by exposing the film to ethanol vapor at 40 °C for 45 minutes. A 0.8 wt. % of iron nitrate ethanolic solution was spin cast on silicon substrate as reported previously.²⁸ For glass and GaN substrates, and to achieve superior etch contrast a 2 wt. % of nickel nitrate ethanolic solution were deposited on the film. UV/Ozone treatment (Novascan PSD series) was used to oxidize the precursor and remove the matrix polymer.

Pattern transfer. Iron oxide nanodots fabricated on substrate surface from BCP template were used as an etch mask for pattern transfer. The silicon etch was performed using C₄F₈ (90 sccm) and SF₆ (30 sccm) gases for various duration of time with an inductively coupled plasma (ICP) and reactive ion etching (RIE) powers of 600 W and 15 W, respectively, at 2.0 Pa with a helium backside cooling pressure of 1.3 kPa to transfer the patterns into the underlying substrate. The

GaN etch was performed using CH₄ (5 sccm), H₂ (15 sccm) and Ar (25 sccm) gases for desired time with ICP and RIE powers of 500W and 45W. The glass etch was performed using Ar (45 sccm) and SF₆ (5 sccm) gasses for 2 min etch time with ICP and RIE powers of 900 W and 100 W respectively. The etching process was accomplished in an OIPT Plasmalab System100 ICP180 etch tool. Figure S4 shows the schematic of the steps for the fabrication of nanopillars.

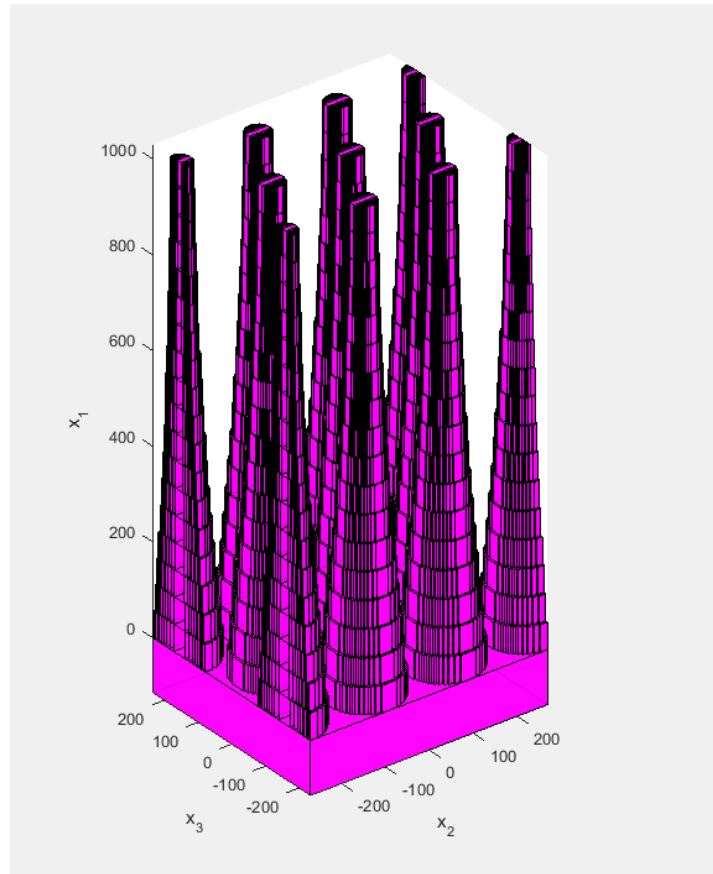
Optical analysis. Angle-resolved optical characterization was conducted using an in-house constructed cage-mounted optical reflectance/transmission spectroscopy setup. The reflectivity was obtained at variable AOI using a rotating sample stage and collection arm with constant path length. Samples were illuminated with a white Halogen bulb collimated to a beam diameter of ~ 1 - 2 mm. UV-Vis-NIR spectra of the reflected light was collected using collimation and focusing optics to two Oceanoptics spectrometers, a USB2000+ and a NIRQuest256-2.5, with optical resolutions of 1.5 nm and 9.5 nm respectively. Reference spectra were acquired using an Au mirror (ThorLabs gold mirror PF10-03-M01) at each AOI investigated prior to sample data collection under identical conditions.

Dimensional analysis. The analysis of the patterns was performed using an in-house algorithm based on the circular Hough transform and Delaunay triangulation. The extracted dimensions were fitted to a Gaussian plot to record the mean and deviation. This methodology allows us to finely measure dimensional information such as cylinder diameter and centre to centre distance (L_0) to monitor the block copolymer patterns. More information is provided in the Supplementary Information (Figure S5).

3D model. Representative 3D models were created in "Rhinceros 5" modelling software. The profile from cross-sectional STEM images was combined with position and outlines from AFM images to form three dimensional polysurfaces. The model was then colorised to show the layers of materials.

Microscopy. Atomic Force Microscope (SPM, Park systems, XE-100) was operated in AC (tapping) mode under ambient conditions using silicon microcantilever probe tips with a force constant of 42 N/m and a scanning force of 0.11 nN. Topographic and phase images were recorded simultaneously. SEM images were obtained by a high resolution (<1 nm) Field Emission Zeiss Ultra Plus-SEM with a Gemini column operating at an accelerating voltage of 5 kV. The scanning transmission electron microscope (STEM) lamella specimen were prepared by the Zeiss Auriga-FIB (Carl Zeiss Microscopy Ltd.) with a Cobra ion column having a unique 2.5 nm resolution and were analysed by FEI Titan-TEM operating at an accelerating voltage of 200 kV.

Simulation. Optical reflectivities are simulated using the “Grating Diffraction Calculator” (GD-Calc®), an electromagnetic simulation program that computes diffraction efficiencies of optical grating structures, including biperiodic gratings. The program’s capabilities include a general and flexible grating modelling facility, structure parameterization (with any number of parameters), and unrestricted control over diffraction order selection. Periodic gratings are “block-structured” (or must be defined approximately in terms of a block structured representation), meaning that the grating comprises optically homogeneous regions whose bounding surfaces are planes parallel to a set of primary coordinate planes. Moth eye-type structures are simulated as truncated cones with upper and lower diameters based on the measured structures.



S7. The simulated SiNPs